Bismuth-doping induced red-shifted spectral response of homo-epitaxial MAPbBr$_3$ photodiodes

Yubing Xu; Xin Wang ✉ ; Yuzhu Pan; ShunJie Chai; Jie Wu ⓘ ; Mengrou Wang ⓘ ; Abida Perveen; Damian Chinedu Onwudiwe; Razika Zair Talaighil; Byung Seong Bae ⓘ ; Ying Zhu ⓘ ; Jing Chen; Wei Lei ✉ ⓘ

Check for updates

CrossMark

View Online

Export Citation

AIP Publishing

Bismuth-doping induced red-shifted spectral response of homo-epitaxial MAPbBr$_3$ photodiodes

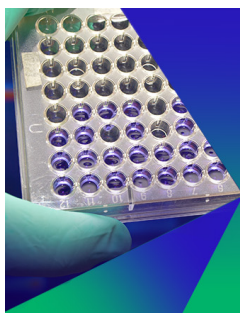View Online   Export Citation   CrossMark

Yubing Xu,[1] Xin Wang,[1,a)] Yuzhu Pan,[1] ShunJie Chai,[1] Jie Wu,[1] (ID) Mengrou Wang,[1] (ID) Abida Perveen,[1] Damian Chinedu Onwudiwe,[2] Razika Zair Talaighil,[3] Byung Seong Bae,[4] (ID) Ying Zhu,[5] (ID) Jing Chen,[1] and Wei Lei[1,a)] (ID)

AFFILIATIONS

[1] School of Electronic Science and Engineering Joint International Research Laboratory of Information Display and Visualization, Southeast University, Nanjing 210000, China

[2] Department of Chemistry, School of Mathematics and Physical Sciences Faculty of Natural and Agricultural Sciences, North-West University, Mafikeng Campus, Private Bag X2046, Mmabatho 2735, South Africa

[3] Institute of Electrical and Electronic Engineering, M'hamed Bougara University of Boumerdes, Boumerdes 35000, Algeria

[4] Department of Electronics and Display Engineering, Hoseo University, Hoseo Ro 79, Asan City, Chungnam 31499, Republic of Korea

[5] E-xray Electronic Co. Ltd., Suzhou, China

a) Authors to whom correspondence should be addressed: xinw@seu.edu.cn and lw@seu.edu.cn

ABSTRACT

Perovskite single crystals (PSCs) photodiodes with p–n junctions have been widely studied due to their effective blocking of injected current with barriers and quickly separating the electrons and hole pairs with a built-in electric field. Here, we report a solution-processed epitaxial (SPE) growth method to fabricate p–n photodiodes based on MAPbBr$_3$ PSCs. In the structure of the MAPbBr$_3$ PSCs, bismuth donor doping will change the conduction type from p-type to n-type and redshift the absorption edge along with the increase in Bi concentration. Therefore, this work successfully fabricates the p–n photodiodes with homo-epitaxial Bi-doped (n-type) MAPbBr$_3$ layers grown on the surface of undoped (p-type) MAPbBr$_3$ PSCs substrates through the SPE growth method. The p–n photodiodes achieve a tunable spectral response by simply adjusting the Bi doping concentrations of homo-epitaxial MAPbBr$_3$ layers. The spectral response peaks redshift from 559 to 601 nm, with an increasing Bi doping level of 0% to 15%.

INTRODUCTION

Recently, organic-inorganic hybrid perovskites (OIHPs), with a chemical formula of MAPbX$_3$ (where MA is CH$_3$NH$_3$, X is Cl, Br, or I), have been highly researched due to their remarkable performance in solution-process based devices such as photodetectors,[1] light-emitting diodes,[2] lasers,[3] and solar cells.[4] Specifically, when compared with perovskite polycrystalline films, perovskite single crystals (PSCs) have lower trap density, longer diffusion length, higher carrier mobility, and more stable performance,[5,6] which shows their great potential for visible light, infrared light, high-energy ray detection, and so on.[7,8]

To fabricate high-performance PSCs-based photodetectors, devices with p–n junctions have been widely used. This extensive usage is due to their ability to effectively block the injected current with barriers and the fast separation of the electrons and hole pairs with the built-in electric field.[9,10] Moreover, when p–n photodiodes work at reverse bias, the depletion region of p–n junctions will be broadened, which benefits the collection of photo-generated carriers. As reported in many works, PSCs-based photodiodes with p–n junctions are fabricated with organic materials, carbon derivatives, and nano-oxides as blocking layers using the spin-coating method, vapor-phase epitaxy, and inkjet printing.[11–13] However, the lattice mismatches between PSCs substrates and the blocking layers are

unavoidable. The poor quality of the blocking layers and the defects that exist in the interface result in a higher leakage of dark currents and noise currents in PSCs devices.

In our previous studies, high-quality PSCs films can be epitaxially grown on homogeneous perovskite substrates or heterogeneous lattice-matched perovskite substrates during the crystallization process, which was named the solution-processed epitaxial (SPE) growth method.[14] Due to the good lattice match, this SPE growth method can be used to fabricate high-performance PSCs photodiodes with p–n junctions. As shown in reported works, Bi donor doping for MAPbBr$_3$ PSCs narrows their bandgaps, changes their conduction type from p-type to n-type, and broadens their absorption ranges.[15,16] Furthermore, the absorption edge of Bi-doped MAPbBr$_3$ PSCs will be redshifted in direct proportionality with increasing Bi doping levels, which results from the generation of trap states induced by impurity doping.

Here, we fabricated p–n photodiodes based on epitaxial grown Bi-doped (n-type) MAPbBr$_3$ layers with different concentrations from 1% to 15% on undoped (p-type) MAPbBr$_3$ PSCs substrates by the SPE growth method. Compared with devices only based on undoped MAPbBr$_3$ PSCs, these p–n photodiodes show redshifted responses due to the broadened absorption ranges of epitaxial Bi-doped MAPbBr$_3$ layers. Moreover, these p–n photodiodes have specific photoresponse peaks from 559 to 601 nm with an increasing Bi concentration from 0% to 15%. In addition, the photodiodes with 10% Bi-doped epitaxial MAPbBr$_3$ layers exhibited the fastest response speed at the level of a meter second and the highest responsivity of 29.1 mA W^{-1} working at −50 V bias.

EXPERIMENTAL METHODS

Materials

Methylammonium bromide (MABr) was obtained by mixing hydrobromic acid (55 wt. % in water, Macklin) with methylamine (30–33 wt. % in ethanol, Macklin). Lead bromide (PbBr$_2$, 99%) and bismuth bromide (BiBr$_3$, 99.9%) were obtained from Sigma-Aldrich, USA. Dimethylformamide-d7 (DMF) was purchased from Macklin. All commercial reagents were used as received.

METHODS

Fabrication of single crystals devices

To grow high-quality MAPbBr$_3$ PSCs as substrates, 1 mol l^{-1} MABr and 1 mol l^{-1} PbBr$_2$ were dissolved in 50 ml of DMF solution to prepare the precursor. According to the inverse temperature crystallization method, the precursor of MAPbBr$_3$ was heated at a rate of 0.3 °C/h from 60 to 80 °C for the high-quality single crystal. To obtain Bi-doped n-type MAPbBr$_3$ precursor, 0.01, 0.05, 0.1, and 0.15 mol l^{-1} BiBr$_3$ were added to the as-prepared MAPbBr$_3$ precursor solution, respectively. In this work, no crystals of regular shape could be crystallized when the doping concentration of the precursor exceeded 15%. The epitaxial single-crystal Bi-doped n-type MAPbBr$_3$ layers were grown by dipping MAPbBr$_3$ single crystals into MAPbBr$_3$ precursor solution with various doping levels. After the epitaxial growth process, the perovskite single crystals were cut by diamond wire (φ0.35 mm) and polished by diamond powder (φ0.5 μm) and a toluene mixed solution. After cutting and polishing

the two-layer crystals, the golden electrodes were deposited on the top and bottom surfaces of single crystals by thermal evaporation in a vacuum.

Characterization of single crystals devices

A UV–vis spectrophotometer (UV-1780, Japan) was used to characterize the absorption of MAPbBr$_3$ single crystals, and the photoluminescence (PL) spectrum and PL decay processes were measured by a SpectraMax instrument (UK). X-ray diffraction (XRD) patterns were obtained by the X'TRA system with a Cu target (Switzerland). Scanning electron microscope (SEM) images were taken with a Quanta 200 FEI (USA), a Transmission Electron Microscope (TEM) image was obtained by a Titan 80–300 FEI (USA), and a high-resolution-transmission electron microscope (HR-TEM) image was obtained by a JEM-200CX (Japan). The major carrier densities of MAPbBr$_3$ single crystals were measured by the Hall effect measurement system (PM-50 MR Plat-form, EMT-2400 Data Acquisition System). The cutting and polishing machines (STX-202A and UNIPOL-1203) were obtained from Shenyang Kejing Auto-instrument Co., Ltd. (Shenyang, China).

RESULTS AND DISCUSSION

This work fabricated undoped and 1%–15% Bi-doped MAPbBr$_3$ PSCs by the inverse temperature crystallization method.[17] It is clearly shown in Fig. 1(a) that the color of MAPbBr$_3$ PSCs darkens with the Bi doping level increasing from 0% to 15%. The absorption edge in Fig. 1(b) shows an apparent redshift from 569 nm for undoped MAPbBr$_3$ PSCs to 665 nm for 15% Bi-doped MAPbBr$_3$ PSCs. Additionally, the red-shifting absorption edge and the Urbach tails in the absorption spectra can be attributed to the formation of the defect states introduced by Bi-doping.[18] Furthermore, the Kubellka–Munk equation was used to calculate the bandgap of crystals, and the formula is

$$(\alpha h\nu)^2 = A(h\nu - E_g),\qquad(1)$$

where α is the absorption coefficient and $h\nu$ is the incident photo energy.[19] Figure 1(c) displays the plot of $(\alpha h\nu)^2$ vs photo energy ($h\nu$). The bandgaps of undoped MAPbBr$_3$ PSCs and 1%, 5%, 10%, and 15% Bi-doped MAPbBr$_3$ PSCs were calculated to be 2.18, 2.01, 1.95, 1.89, and 1.86 eV, respectively. The narrowed bandgap of the Bi-doped single crystal has been ascribed to the density of states induced by Bi^{3+} doping.[20] The XRD patterns of undoped and Bi-doped MAPbBr$_3$ PSCs are shown in Fig. 1(d). It is clearly shown in XRD patterns that no extra peaks exist after Bi-doping, and the calculated lattice constants of Bi-doped PSCs are consistent with undoped MAPbBr$_3$ PSCs.[21] Bi-doping retains the lattice structure of MAPbBr$_3$ perovskite due to the very similar ionic radius of Bi^{3+} (1.03 Å) and Pb^{2+} (1.19 Å). As evident in Fig. 1(e), the PL spectra of Bi-doped MAPbBr$_3$ PSCs have a slight red shift of band-edge emission, indicating that impurity levels are formed by Bi^{3+} doping. What is more, the trap states induced by Bi^{3+} doping increase non-radiative recombination, which causes a large decrease in PL intensity with respect to undoped MAPbBr$_3$ PSCs.[22] In addition, Fig. 1(f) exhibits the time-resolved PL decay of MAPbBr$_3$ PSCs with different Bi doping concentrations and suggests that the carrier lifetime calculated by a double exponential fitting decreases with
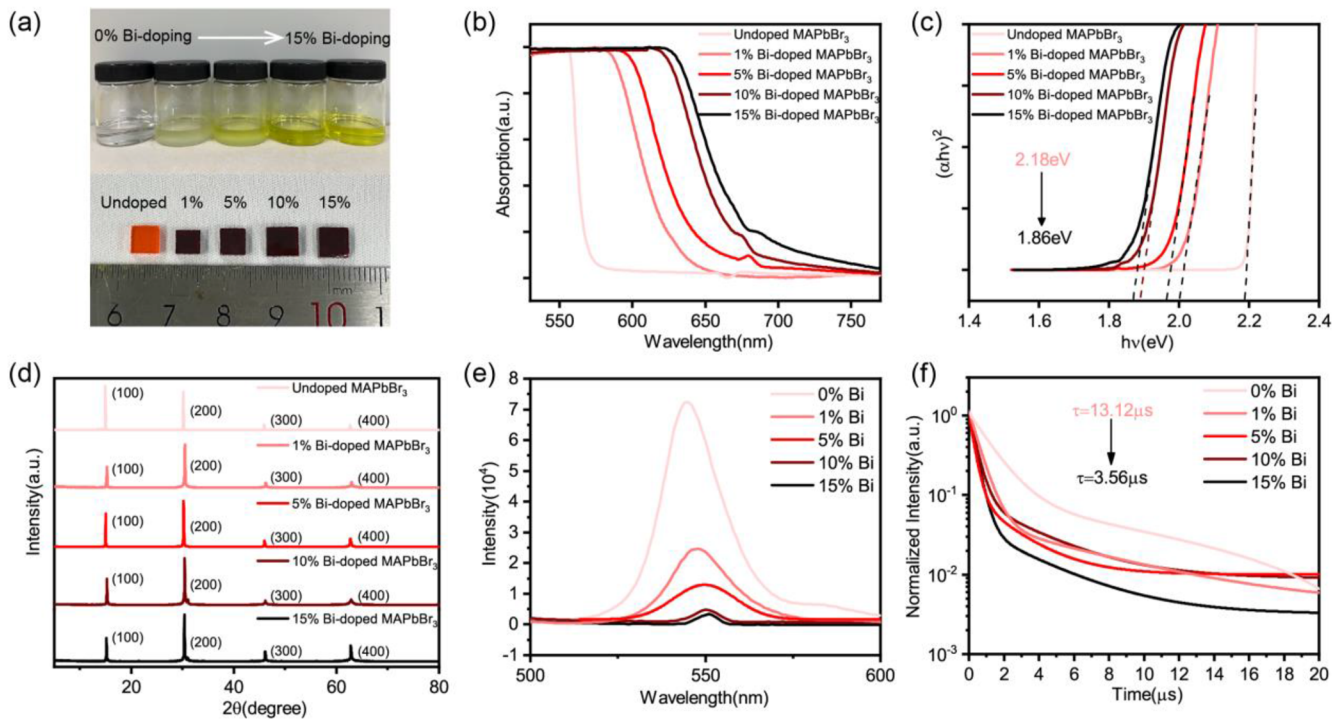
FIG. 1. Optical properties of MAPbBr$_3$ PSCs with various Bi doping concentrations range from 0% to 15%. (a) Pictures of MAPbBr$_3$ precursor solution and single crystals with various Bi doping levels. (b) Normalized absorption spectra of undoped and Bi-doped MAPbBr$_3$ PSCs at different Bi ion concentrations. (c) Corresponding Tauc plots of undoped and Bi-doped MAPbBr$_3$ PSCs at different concentrations. (d) X-ray diffraction (XRD) patterns of undoped and Bi-doped MAPbBr$_3$ PSCs. (e) Steady-state photoluminescence (PL) spectrum of undoped and Bi-doped MAPbBr$_3$ PSCs. (f) Time-resolved photoluminescence (TRPL) of undoped and Bi-doped MAPbBr$_3$ PSCs.

an increase in the Bi dopant concentration. The trap states introduced by Bi enhanced the carrier trapping, resulting in a decreasing lifetime.[23]

To further study the effect introduced by Bi dopants, Hall effect measurement was used to characterize the conduction type and the major carrier density of MAPbBr$_3$ PSCs with various Bi%.[24] As shown in Fig. 2(a), the incorporation of Bi into MAPbBr$_3$ PSCs changes their conduction type from p-type to n-type. Moreover, the major carrier density will increase with Bi dopants concentration. By calculating the average value of 5 magnet rotation cycles, the majority carrier density of 15% Bi-doped MAPbBr$_3$ is 2.71 × 10^{17} cm^{-3}, and that of 10% Bi-doped MAPbBr$_3$ is 1.13 × 10^{11} cm^{-3}. In addition, for n-type semiconductor materials, the distance between the intrinsic Fermi level (E_{Fi}) and the Fermi level (E_F) can be calculated using the following formula:

$$E_F - E_{Fi} = kT \ln \frac{n_0}{n_i}, \qquad (2)$$

where k is the Boltzmann constant, T is temperature, n_0 is the electron concentration at thermal equilibrium, and n_i is the intrinsic carrier concentration. Figure 2(b) displays the bandgap alignment of MAPbBr$_3$ PSCs with various Bi% according to their electrical and optical properties. Summarily, heterovalent doping narrows the bandgap, does not change the lattice structure, changes the conduction type, and tunes the electrical properties of MAPbBr$_3$ PSCs,

which offers a new path for the fabrication and development of PSC-based devices. Herein, we take advantage of Bi-doped (n-type) MAPbBr$_3$ PSCs of consistent lattice constant with undoped (p-type) MAPbBr$_3$ to fabricate p–n photodiodes. The solution-processed epitaxial (SPE) growth process is shown in Fig. 2(c). First, the MAPbBr$_3$ PSCs were grown by the inverse temperature crystallization method as high-quality substrates. Then, the substrate single crystals were put into a Bi-doped MAPbBr$_3$ precursor solution at 65 °C. Due to the good lattice match between homojunctions, the homo-epitaxial single-crystal Bi-doped (n-type) MAPbBr$_3$ layers can be easily grown on the surface of undoped (p-type) MAPbBr$_3$ substrates. After the cutting and polishing process, the two-layer homostructure was successfully fabricated. The thickness of epitaxial layers can be controlled consistently by the cutting and polishing processes. The pictures in Fig. 2(d) show the surface and their related cross-section of two-layer homostructure single crystals with various Bi concentrations. The color of homo-epitaxial single-crystal MAPbBr$_3$ layers darkens with the concentration of Bi. Take homostructure with 10% Bi-doped MAPbBr$_3$ layers, for example. Fig. 2(e) shows the scanning electron microscopy (SEM) image of the surface of the epitaxial single-crystal layer at a 5 μm scale. Additionally, the cross-sectional images at 400 and 5 μm in Fig. 2(f) show the thickness and the interface between substrates and homo-epitaxial layers. As shown in Fig. 2(f), the thickness of the epitaxial Bi-doped MAPbBr$_3$ crystal layer is about 300 μm. The HRTEM image in Fig. 2(f) reveals a
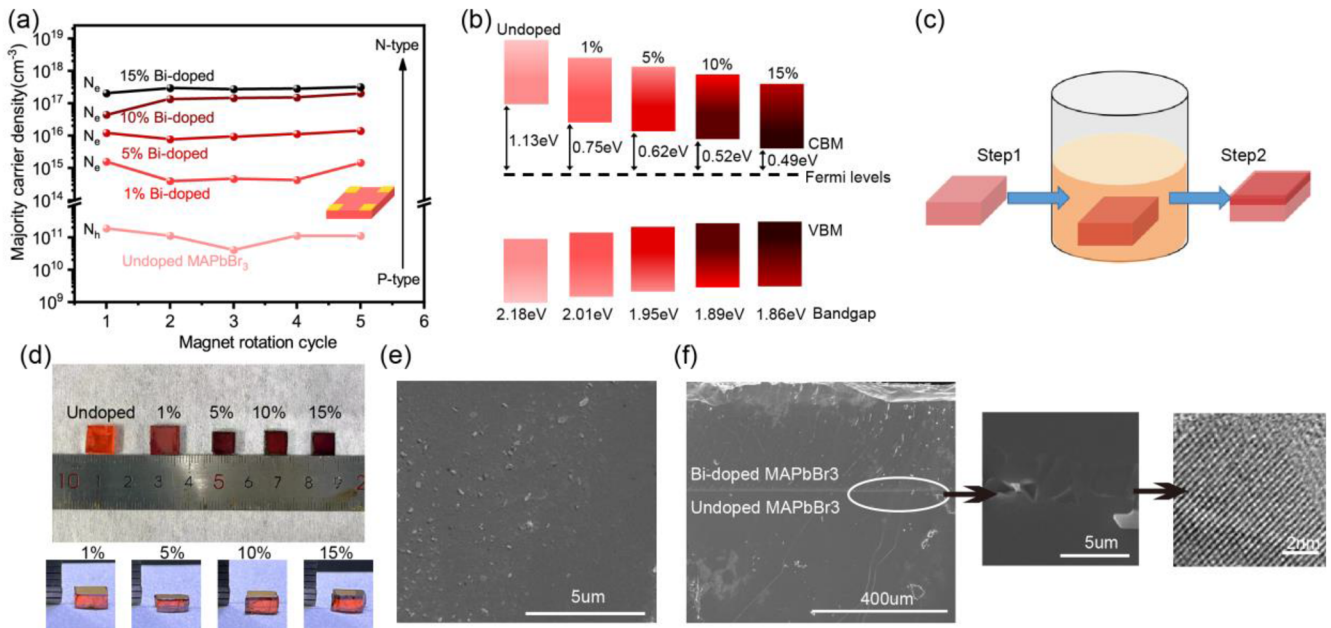
FIG. 2. Fabrication of p–n photodiodes based on homo-epitaxial single-crystal Bi-doped MAPbBr$_3$ layers. (a) Hall effect results reveal the majority carrier density and conduction type of undoped and Bi-doped MAPbBr$_3$ PSCs. (b) Bandgap alignment of MAPbBr$_3$ PSCs with various Bi%. (c) The diagram of the solution-processed epitaxial (SPE) growth method. (d) Pictures of MAPbBr$_3$ PSCs with homo-epitaxial single-crystal Bi-doped MAPbBr$_3$ layers at different concentrations after SPE growth and their cross-section after cutting and polishing. (e) Scanning electron microscope (SEM) image showing the surface of a homo-epitaxial single-crystal 10% Bi-doped MAPbBr$_3$ layer. The scale bar is 5 μm. (f) SEM images showing the cross-section of a homo-epitaxial single-crystal 10% Bi-doped MAPbBr$_3$ layer on an undoped MAPbBr$_3$ substrate. The scale bars are 400 and 5 μm, respectively. In addition, a high-resolution transmission electron microscope (HRTEM) image shows the interfacial area of the homo-epitaxial single-crystal layer. The scale bar is 2 nm.

well-aligned cubic lattice between substrates and homo-epitaxial layers without dislocations.[25] In conclusion, benefiting from the good lattice match, the homo-epitaxial single-crystal Bi-doped (n-type) MAPbBr$_3$ layers fabricated by SPE growth methods have a compact surface, controllable thickness, and excellent interface, which are favorable to the high performance of the p–n photodiodes.

To further characterize the performance of our p–n photodiodes based on homo-epitaxial single-crystal n-type MAPbBr$_3$ layers, two gold electrodes were deposited on the opposite surfaces of single crystals, which formed the Au/n-type MAPbBr$_3$/p-type MAPbBr$_3$/Au structure. Figure 3(a) shows the dark I–V curve of p–n photodiodes with various Bi doping levels of 1%, 5%, 10%, and 15%, respectively. The typical rectifying behaviors in Fig. 3(a) are ascribed to p–n junctions formed near the interfaces. For impurity doping, the SCLC method was used to characterize the trap density of our p–n photodiodes.[26,27] The formula is

$$n_{traps} = \frac{(2\varepsilon V_{TFL})}{qL^2},\tag{3}$$

where ε is the relative dielectric constant, V_{TFL} is the trap-filled limit voltage at which all injected charge carriers are used to fill all traps, q is the electronic charge, and L is the distance between the opposite electrodes. The calculated trap densities of p–n photodiodes at various Bi doping levels are shown in Figs. 3(b)–3(e). The working principle of p–n junction-based devices under reverse voltage bias is displayed in Fig. 3(f). After n-type layers come into contact

with p-type substrates, electrons will diffuse from n-type material to p-type material, while holes will diffuse in the opposite direction, and a depletion layer will be formed near the interface. When working under reverse voltage bias, the depletion area will be broadened, which enhances light absorption and the effective separation of photo-generated carriers. Under illumination, photo-generated electrons will drift to n-type MAPbBr$_3$, while photo-generated holes will drift to p-type MAPbBr$_3$. Meanwhile, the high barriers between perovskite and gold can block injected holes and electrons.

Furthermore, the spectral photoresponse was characterized here to compare the photodiodes based on Au/n-type MAPbBr$_3$/p-type MAPbBr$_3$/Au structure with the device based on Au/p-type MAPbBr$_3$/Au. As mentioned earlier [Fig. 1(b)], the absorption edge of Bi-doped MAPbBr$_3$ PSCs was red-shifted along with the increasing Bi-doping level, which indicates the formation of trap states introduced by impurity doping. In this case, the homo-epitaxial single-crystal Bi-doped MAPbBr$_3$ layers of the p–n photodiodes will absorb visible light at longer wavelengths. The photo-generated carriers in the drift area will be separated and collected under reverse bias. The normalized EQE spectra of photodiodes with 1%, 5%, 10%, and 15% Bi-doped homo-epitaxial MAPbBr$_3$ layers compared with undoped MAPbBr$_3$ PSCs-based photodetectors are shown in Fig. 4(a). It is evident that the spectral response peak of photodiodes with 1%–15% Bi-doped MAPbBr$_3$ layers shifted to a longer wavelength from 559 to 601 nm with increasing concentrations of Bi-doping from 0% to 15%. Compared to previously reported studies involving undoped MAPbBr$_3$ photodetectors,[28,29] the p–n photo-
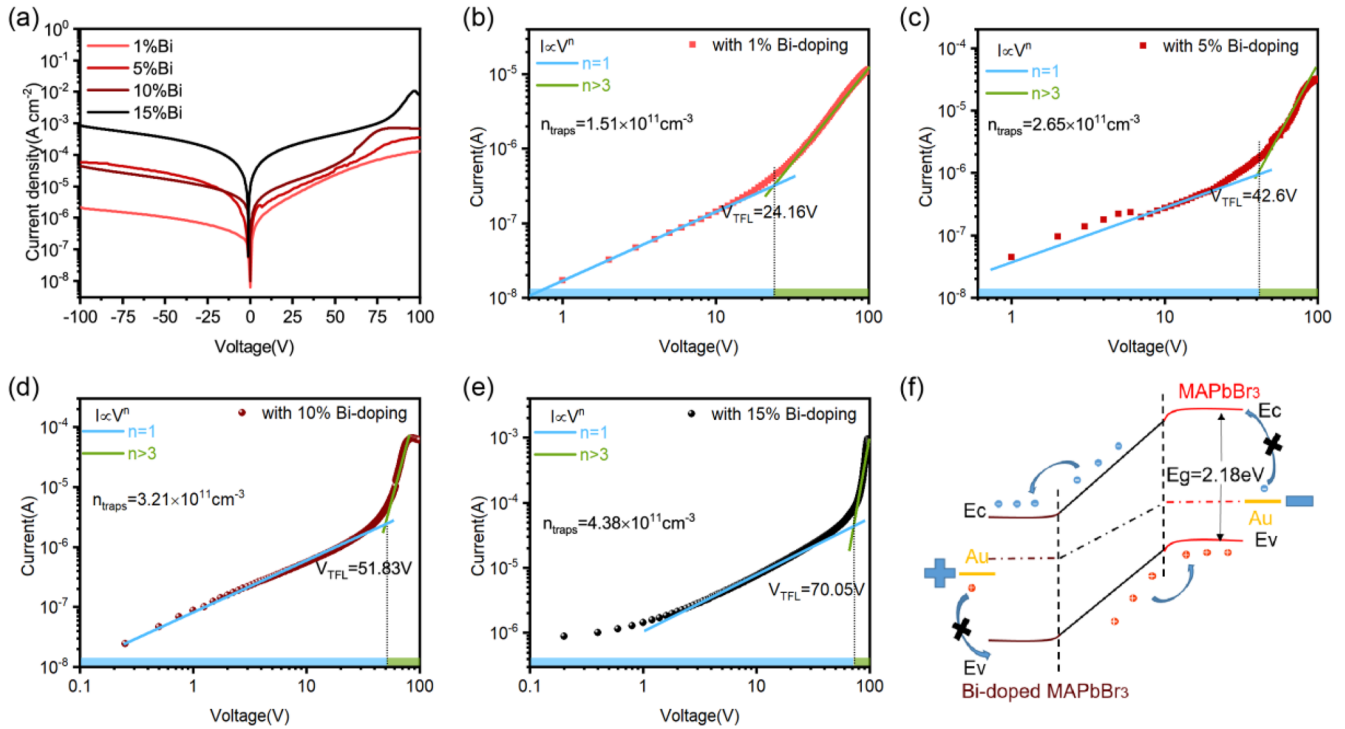
FIG. 3. Basic characterization of the photodiodes with Bi-doping induced trap states. (a) Dark current densities of p–n photodiodes with homo-epitaxial single-crystal n-type MAPbBr$_3$ layers at different concentrations. (b)–(e) The trap densities of p–n photodiodes with homo-epitaxial single-crystal n-type MAPbBr$_3$ layers with 1%–5% Bi-doping were measured by the space-charge-limited-currents (SCLCs) method. (f) Schematic diagrams illustrating the working principles of this p–n photodiode under reverse working bias.
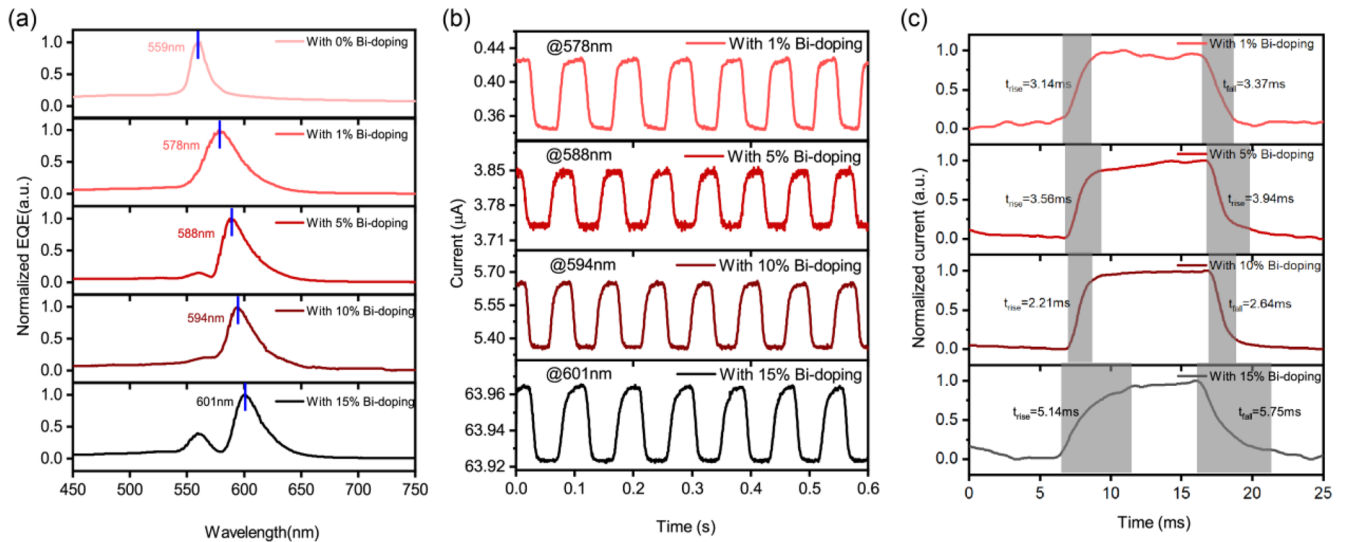

FIG. 4. Spectral photoresponse of the photodiodes with 1%–15% Bi-doped n-type MAPbBr$_3$ layers. (a) Normalized external quantum efficiency (EQE) spectra of an undoped MAPbBr$_3$ PSCs-based detector and p–n photodiodes with homo-epitaxial single-crystal n-type MAPbBr$_3$ layers at different concentrations. Their response peaks have a clear redshift. (b) Temporal photoresponse of p–n photodiodes with 1%–15% Bi-doped n-type MAPbBr$_3$ layers at their peak spectral wavelength. (c) Response time of p–n photodiodes with 1%–15% Bi-doped n-type MAPbBr$_3$ layers.

diodes reported here with Bi-doped MAPbBr$_3$ layers show clear red-shifted spectral response peaks. Figure 4(b) shows the temporal photoresponse of different Bi-doped photodiodes at their peak spectral wavelength at −50 V bias. Their responsivities (R) are calculated by the formula

$$R = \frac{(I_{ON} - I_{OFF})}{(P_{light} \times S)},\qquad (4)$$

where S is the effective area and P_{light} is the light intensity.[30] The calculated R of the photodiodes at −50 V bias with 1%, 5%, 10%, and 15% Bi-doped homo-epitaxial MAPbBr$_3$ layers are 8.1 mA W^{-1} at 578 nm, 10.6 mA W^{-1} at 588 nm, 29.1 mA W^{-1} at 594 nm, and 4.38 mA W^{-1} at 601 nm, respectively. What is more, the response speed is also a significant property for photodiodes which is defined here as the rise and fall time taken for photocurrent to increase from 10% to 90% of the peak value and vice versa.[31] As displayed in Fig. 4(c), photodiodes with 10% Bi-doped n-type MAPbBr$_3$ layers have the shortest rise time of 2.21 ms and the shortest fall time of 2.64 ms. Therefore, the photodiodes based on homo-epitaxial single-crystal 10% Bi-doped MAPbBr$_3$ layers have the fastest rise and fall time and the highest responsivity.

CONCLUSIONS

In summary, this work fabricated p–n photodiodes based on homo-epitaxial n-type MAPbBr$_3$ layers with various Bi doping levels through the solution-processed epitaxial growth method. These p–n photodiodes displayed a tunable and red-shifted spectral response by simply varying the concentration of the Bi dopants in homo-epitaxial layers. The spectral response peak shifted to a longer wavelength from 559 to 601 nm with increasing Bi-doping concentrations from 0% to 15%. Additionally, the photodiodes with 10% Bi-doped homo-epitaxial MAPbBr$_3$ layers have the highest responsivity of 29.1 mA W^{-1} and the fastest response time of 2.21/2.64 ms at 594 nm. Overall, this study offers a new path to fabricate perovskite-based photodiodes with tunable spectral responses for applications of specific wavelength detection.

ACKNOWLEDGMENTS

AUTHOR DECLARATIONS

Conflict of Interest

The authors have no conflicts to disclose.

Author Contributions

Yubing Xu: Investigation (equal); Writing – original draft (equal). **Xin Wang**: Writing – review & editing (equal). **Yuzhu Pan**: Investigation (equal). **ShunJie Chai**: Investigation (equal). **Jie Wu**: Methodology (equal). **Mengrou Wang**: Investigation (equal). **Abida Perveen**: Investigation (equal). **Damian Chinedu Onwudiwe**: Writing – review & editing (equal). **Razika Zair Talaighil**: Writing – review & editing (equal). **Byung Seong Bae**: Writing – review & editing (equal). **Ying Zhu**: Writing – review & editing (equal). **Jing Chen**: Methodology (equal). **Wei Lei**: Writing – review & editing (equal).

DATA AVAILABILITY

The data that support the findings of this study are available within the article.

REFERENCES

[1] Y. Fang, Q. Dong, Y. Shao, Y. Yuan, and J. Huang, Nat. Photonics **9**, 679 (2015).

[2] H. Cho, S. H. Jeong, M. H. Park, Y. H. Kim, C. Wolf, C. L. Lee, J. H. Heo, A. Sadhanala, N. Myoung, S. Yoo, S. H. Im, R. H. Friend, and T. W. Lee, Science **350**, 1222 (2015).

[3] H. Zhu, Y. Fu, F. Meng, X. Wu, Z. Gong, Q. Ding, M. V. Gustafsson, M. T. Trinh, S. Jin, and X. Y. Zhu, Nat. Mater. **14**, 636 (2015).

[4] N. J. Jeon, J. H. Noh, W. S. Yang, Y. C. Kim, S. Ryu, J. Seo, and S. I. Seok, Nature **517**, 476 (2015).

[5] W. Wang, H. Meng, H. Qi, H. Xu, W. Du, Y. Yang, Y. Yi, S. Jing, S. Xu, F. Hong, J. Qin, J. Huang, Z. Xu, Y. Zhu, R. Xu, J. Lai, F. Xu, L. Wang, and J. Zhu, Adv. Mater. **32**, 2001540 (2020).

[6] D. Shi, V. Adinolfi, R. Comin, M. Yuan, E. Alarousu, A. Buin, Y. Chen, S. Hoogland, A. Rothenberger, K. Katsiev, Y. Losovyj, X. Zhang, P. A. Dowben, O. F. Mohammed, E. H. Sargent, and O. M. Bakr, Science **347**, 519 (2015).

[7] J. Zhou and J. Huang, Adv. Sci. **5**, 1700256 (2018).

[8] J. Li, Z. Han, Y. Gu, D. Yu, J. Liu, D. Hu, X. Xu, and H. Zeng, Adv. Funct. Mater. **31**, 2008684 (2020).

[9] F. Liu, M. Yoho, H. Tsai, K. Fernando, J. Tisdale, S. Shrestha, J. K. Baldwin, A. D. Mohite, S. Tretiak, D. T. Vo, and W. Nie, Mater. Today **37**, 27 (2020).

[10] X. Wang, Y. Xu, Y. Pan, Y. Li, J. Xu, J. Chen, J. Wu, Q. Li, X. Zhang, Z. Zhao, C. Li, E. E. Elemike, D. C. Onwudiwe, J. Akram, and W. Lei, Nano Energy **89**, 106311 (2021).

[11] Z. Lan, L. Cai, D. Luo, and F. Zhu, ACS Appl. Mater. Interfaces **13**, 981 (2021).

[12] Y. Chen, M. He, J. Peng, Y. Sun, and Z. Liang, Adv. Sci. **3**, 1500392 (2016).

[13] K. Kimura, Y. Nakamura, T. Matsushita, and T. Kondo, Jpn. J. Appl. Phys. **58**, SBBF04 (2019).

[14] Y. Xu, X. Wang, J. Zhao, Y. Pan, Y. Li, E. E. Elemike, Q. Li, X. Zhang, J. Chen, Z. Zhao, J. Akram, B. S. Bae, S. Bin, and W. Lei, Front. Mater. **8**, 107 (2021).

[15] A. L. Abdelhady, M. I. Saidaminov, B. Murali, V. Adinolfi, O. Voznyy, K. Katsiev, E. Alarousu, R. Comin, I. Dursun, L. Sinatra, E. H. Sargent, O. F. Mohammed, and O. M. Bakr, J. Phys. Chem. Lett. **7**, 295 (2016).

[16] W. Tang, J. Zhang, S. Ratnasingham, F. Liscio, K. Chen, T. Liu, K. Wan, E. S. Galindez, E. Bilotti, M. Reece, M. Baxendale, S. Milita, M. A. McLachlan, L. Su, and O. Fenwick, J. Mater. Chem. A **8**, 13594 (2020).

[17] M. I. Saidaminov, A. L. Abdelhady, B. Murali, E. Alarousu, V. M. Burlakov, W. Peng, I. Dursun, L. Wang, Y. He, G. Maculan, A. Goriely, T. Wu, O. F. Mohammed, and O. M. Bakr, Nat. Commun. **6**, 7586 (2015).

[18] R. Wang, X. Zhang, J. He, C. Ma, L. Xu, P. Sheng, and F. Huang, J. Alloys Compd. **695**, 555 (2017).

[19] F. X. Liang, J. J. Jiang, Y. Z. Zhao, Z. X. Zhang, D. Wu, L. H. Zeng, Y. H. Tsang, and L. B. Luo, Adv. Funct. Mater. **30**, 2001033 (2020).

[20] Z. Zhang, L. Ren, H. Yan, S. Guo, S. Wang, M. Wang, and K. Jin, J. Phys. Chem. C **121**, 17436 (2017).

[21] E. Jedlicka, J. Wang, J. Mutch, Y. K. Jung, P. Went, J. Mohammed, M. Ziffer, R. Giridharagopal, A. Walsh, J. H. Chu, and D. S. Ginger, J. Phys. Chem. Lett. **12**, 2749 (2021).

[22] A. M. Ulatowski, A. D. Wright, B. Wenger, L. R. V. Buizza, S. G. Motti, H. J. Eggimann, K. J. Savill, J. Borchert, H. J. Snaith, M. B. Johnston, and L. M. Herz, J. Phys. Chem. Lett. **11**, 3681 (2020).

[23] R. Begum, M. R. Parida, A. L. Abdelhady, B. Murali, N. M. Alyami, G. H. Ahmed, M. N. Hedhili, O. M. Bakr, and O. F. Mohammed, J. Am. Chem. Soc. **139**, 731 (2017).

[24] Y. Chen, H. T. Yi, X. Wu, R. Haroldson, Y. N. Gartstein, Y. I. Rodionov, K. S. Tikhonov, A. Zakhidov, X. Y. Zhu, and V. Podzorov, Nat. Commun. **7**, 12253 (2016).

[25] Y. Lei, Y. Chen, R. Zhang, Y. Li, Q. Yan, S. Lee, Y. Yu, H. Tsai, W. Choi, K. Wang, Y. Luo, Y. Gu, X. Zheng, C. Wang, C. Wang, H. Hu, Y. Li, B. Qi, M. Lin, Z. Zhang, S. A. Dayeh, M. Pharr, D. P. Fenning, Y. H. Lo, J. Luo, K. Yang, J. Yoo, W. Nie, and S. Xu, Nature **583**, 790 (2020).

[26] J. Pospisil, O. Zmeskal, S. Nespurek, J. Krajcovic, M. Weiter, and A. Kovalenko, Sci. Rep. **9**, 3332 (2019).

[27] E. A. Duijnstee, J. M. Ball, V. M. Le Corre, L. J. A. Koster, H. J. Snaith, and J. Lim, ACS Energy Lett. **5**, 376 (2020).

[28] S. Guo, S. Qiao, J. Liu, J. Ma, and S. Wang, Opt. Express **30**, 11536 (2022).

[29] M. Cao, J. Tian, Z. Cai, L. Peng, L. Yang, and D. Wei, Appl. Phys. Lett. **109**, 233303 (2016).

[30] X. Wu, B. Zhou, J. Zhou, Y. Chen, Y. Chu, and J. Huang, Small **14**, 1800527 (2018).

[31] J. Wang, S. Xiao, W. Qian, K. Zhang, J. Yu, X. Xu, G. Wang, S. Zheng, and S. Yang, Adv. Mater. **33**, 2005557 (2021).

28 February 2024 10:22:59